Progress In Electromagnetics Research C, Vol. 129, 257–271, 2023

Multi-Objective Optimization Design of ERSRM with Asymmetric Stator Poles

Chaozhi Huang, Hongwei Yuan*, Wensheng Cao, and Yuliang Wu

Abstract—This paper proposes a novel asymmetric interior stator topology for torque enhancement and torque ripple reduction in external rotor switched reluctance motor (ERSRM). The new topology and operational principle are first investigated using a simplified linear model. Then, the parametric model of the ERSRM and the comprehensive sensitive analysis that evaluates the influence of each design variable on optimization objectives are presented. Thirdly, the optimal design is selected from the Pareto front which is generated by NSGA-II (fast non-dominated sorting genetic algorithm) and validated by finite element analysis. Finally, the optimal prototype motor is manufactured, and experimental results confirm the validity and superiority of the optimized design.

1. INTRODUCTION

As a light-weight, fast, and very clean mode of transportation, electric bicycles (E-bikes) can relieve the pressure of traffic and attract a great attention [1]. Switched reluctance motor (SRM) is suitable for E-bikes hub motor due to its simple structure, high drive reliability, and no use of permanent magnet materials [2]. However, the torque ripple of SRM affects the driving experience of the E-bikes, reducing the torque ripple, and vibration noise has become the necessary problem of the application of SRM [3].

The combination of poles and slots in SRM has a great effect on output performances such as torque ripple and efficiency. For interior rotor SRM, 6/4, 6/8, and 6/10 configurations have been evaluated in [4]. The average torque, torque density, and single-phase loss are positively correlated with torque to the rotor pole number, and the torque ripple is negatively correlated with to the rotor pole number for three-phase SRM. For the external rotor SRM(ERSRM), 12/8 and 12/16 configurations have been evaluated in [5], and the 12/8 structure has higher efficiency under the same control parameters, while the 12/16 structure has lower torque ripple.

Modifying the stator or rotor pole shape of SRM to change the air gap magnetic flux distribution can reduce torque ripple. The influence of different stator and rotor pole shapes on SRM torque ripple is investigated in [6]. A novel segmented-rotor SRM is proposed in [7], with non-integer slot and rotor opening notch used to reduce the torque ripple, and results show that this motor has lower torque ripple than the conventional SRM of same-volume. Ref. [8] has studied the influence of rotor shapes on the average torque and torque ripple. When the angle control strategy is used to control SRM, the turn-on angle (θ_{on}) and turn-off angle (θ_{off}) can be controlled to adjust the winding current of each phase and then control the synthetic torque of the commutation region. A hybrid method of Wingsuit Flying Search (WFS) optimization and Gradient Boosting Decision Tree (GBDT) algorithm was proposed in [9] to optimize θ_{on} and θ_{off} of SRM.

Searching for the best design is not a simple task because SRM has a lot of geometric and control parameters. Many optimization methods for motors have been proposed. A method to reduce the

Received 2 December 2022, Accepted 3 February 2023, Scheduled 12 February 2023
* Corresponding author: Hongwei Yuan (2550747126@qq.com).
The authors are with the College of Electrical and Automation, Jiangxi University of Science and Technology, Ganzhou 341000, China.

torque ripple of induction motor by artificial neural network is proposed in [10]. An optimization design method for a double-stator hybrid excited permanent magnet arc motor (DS-HE-PMAM) is presented in [11]. The authors adopted fast non-dominated sorting genetic algorithm (NSGA-II) and a machine learning algorithm random forest (RF) in order to maximize average torque, back electromotive force (EMF) while minimizing torque ripple and total harmonic distortion of the back EMF. A closed-loop optimization design method that connected the FEA and intelligent algorithm optimizer by the transformation of script files is proposed in [12, 13]. In this way, each calculation step is a closed loop.

In this paper, we investigate the causes of torque ripple of SRM and propose a combined stator structure of pole shoes and deflection auxiliary teeth. The new topology and operational principle are first investigated using a simplified equivalent linear mode model. Then, the parametric model of the ERSRM is established. We adopt a comprehensive sensitivity approach to select the variables that are strongly correlated with the optimization objectives. The NSGA-II and finite element analysis (FEA) are connected by the interface script program to optimize the strongly correlated variables. Finally, the prototype of the optimization result is manufactured to validate the effectiveness of asymmetric structure of suppressing torque ripple.

2. TORQUE RIPPLE ANALYSIS

Generally, the torque ripple formula can be given by:

$$T_{rip} = \frac{T_{\max} - T_{\min}}{T_{avg}} \times 100\% \tag{1}$$

where $T_{\max}$, $T_{\min}$, and T_{avg} are the highest torque, lowest torque, and average torque in a rotor-pitch period, respectively. Raising the minimum torque while reducing the peak torque can greatly reduce the torque ripple.

The minimum torque of SRM is related to the lowest synthetic torque in the commutation interval. As shown in Fig. 1, the minimum torque of the SRM is generated in the first half of the rotor commutation interval $[\theta_{on} \cdot \theta_{z(k+1)}]$. At this time, the front phase torque decreases rapidly, while the latter phase rotor does not provide sufficient torque. Currently, the rotor is near the unaligned position, and the inductance change rate is low. According to Fig. 1, we can advance θ_{on} to raise the latter phase current in advance, thereby raising the lowest synthetic torque in the commutation interval.

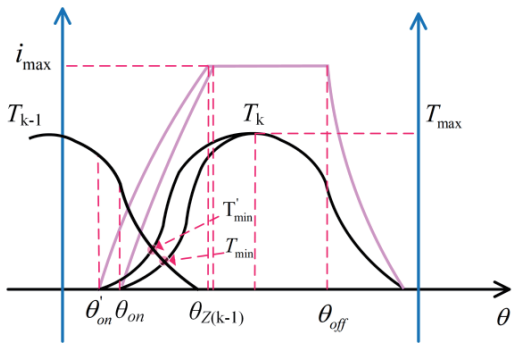

Figure 1. Torque and current curves during commutation.

Under the linear assumption, the electromagnetic torque can be expressed as:

$$T_t = \frac{dW'(i,\theta)}{d\theta} = \frac{1}{2} i^2 \frac{dL(\theta,i)}{d\theta} \tag{2}$$

where W' is the magnetic common energy. (2) indicates the motor torque depends highly on phase current (i) and the changing of motor inductance $L(\theta, i)$ with rotor position angle (θ).

The maximum torque of ERSRM is related to the peak torque of the single phase. According to (2), the torque is proportional to the inductance change rate in the case of constant current amplitude.

If the inductance change rate at the peak torque can be reduced, the purpose of reducing the peak torque can be achieved. The magnetic flux ψ is expressed:

$$\psi = Li = N^2 \Lambda i \tag{3}$$

where N is the number of windings turns. The magnetic flux is proportional to the inductance L and magnetic permeability Λ when the number of windings turns and the current limit value are constant. Therefore, the change rate of inductance can be changed by adjusting the change rate of the magnetic permeability [10].

3. MOTOR STRUCTURE AND OPERATION

3.1. Structure of the ERSRM

Based on the principle of magnetic conductivity adjustment, we propose a new asymmetric stator structure. The configuration of the ERSRM is shown in Fig. 2(a). We add pole shoes in the stator's reverse rotation direction and deflection auxiliary teeth on the stator's positive rotation direction, respectively. The parameterized cross-section in Fig. 2(b) includes 9 design parameters, which are rationalized and confined according to Table 1. Table 1 also includes several important variables such as windings turns, θ_{on} and θ_{off}. These parameters can be further classified into several types. The first type is the initial design parameters. For example, the stator inter and rotor outer radius are fixed to 20 and 105 mm, respectively. They are determined by the initial design of the motor. The second type is the not determined design parameters.

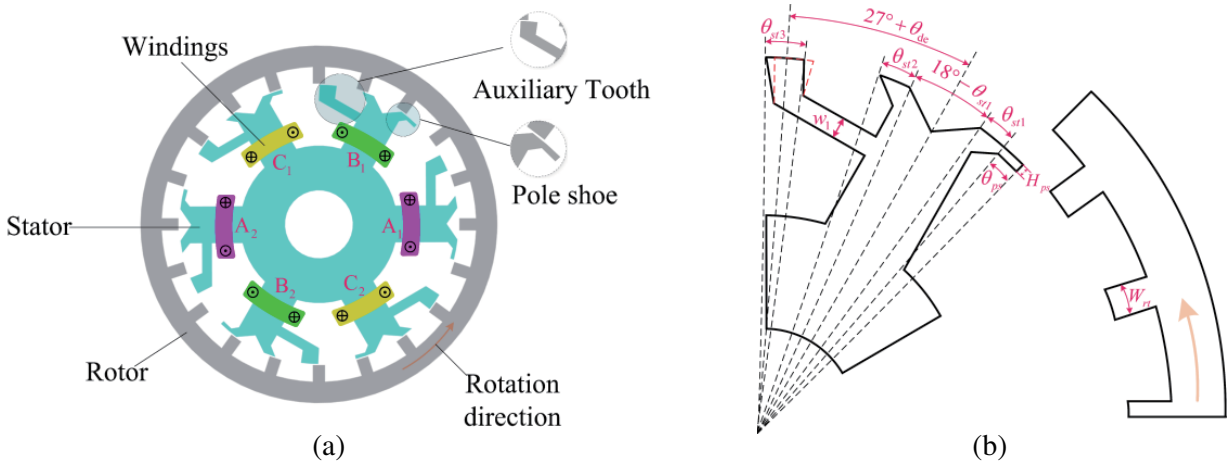

Figure 2. (a) 2-D structure diagram of the ERSRM. (b) Parameterized model of the ERSRM.

3.2. Electromagnetic Principle of Adding Single Pole Shoe

Under the linear assumption, the edge magnetic conductivity effect is ignored, and the leakage of magnetic field is not considered. Fig. 3 shows the simplified diagram of stator-sided pole shoe, where β_r, β_s, β_{shoe} are the arc of rotor tooth, stator tooth, and the pole shoe, respectively.

The air gap magnetic conductivity differential can be expressed as:

$$d\Lambda = \frac{\mu_0}{\delta} dS \tag{4}$$

where μ_0 is the vacuum permeability, δ the air gap length, and dS the differential of the stator and rotor overlap area in air gap region.

When pole shoes are added, the stator pole shoes and rotor poles begin to overlap but not overlap completely, that is $9^\circ - (\frac{\beta_r+\beta_s}{2} + \beta_{shoe}) \cdot \frac{180^\circ}{\pi} < \theta < 9^\circ - (\frac{\beta_r+\beta_s}{2}) \cdot \frac{180^\circ}{\pi}$, the magnetic permeability of

Table 1. Design parameters of the ERSRM.

	Parameters	Description	Unit	Range/Value
Stator parameters	R_{si}	Stator inter radius	mm	20
	R_{syo}	Stator yoke outer radius	mm	46
	w_1	Auxiliary tooth branch width	mm	5–7
	N	Windings turns	turns	30–50
	θ_{ps}	Pole shoe angle	mm	0–3
	H_{ps}	Pole shoe height	mm	0–3
	θ_{st1}	Stator tooth 1 angle	deg	4–5
	θ_{st2}	Stator tooth 2 angle	deg	4–5
	θ_{st3}	Auxiliary tooth 3 angle	deg	5–9
	θ_{de}	Auxiliary tooth deflection angle	deg	−3–1
	h_g	Air gap length	mm	0.7
	R_{ri}	Rotor inter radius	mm	82.7
	R_{ryi}	Rotor yoke inter radius	mm	92.5
Rotor parameters	W_{rt}	Rotor tooth width	mm	6.5–8.5
	R_{ro}	Stator outer radius	mm	105
Control parameters	θ_{on}	Turn on angle	deg	$-1 \sim 1$
	θ_{off}	Turn off angle	deg	$6 \sim 9$

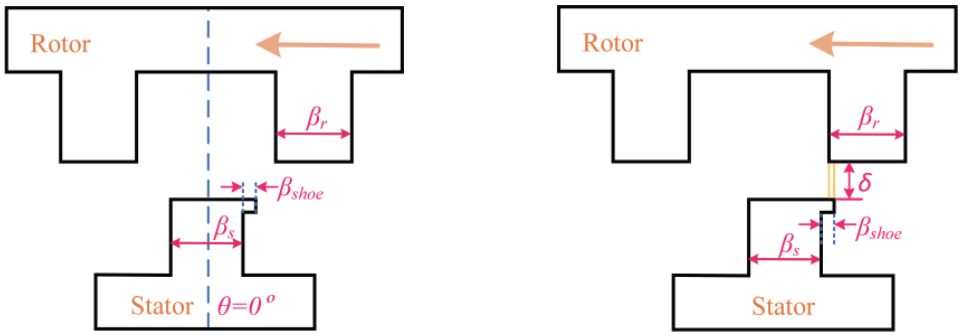

Figure 3. (a) Unaligned position, (b) Partial aligned position.

the structure with pole shoes is greater than the magnetic permeability of the structure with no pole shoes. The inductance and flux linkage on the non-overlapping region can be effectively increased with increasing the magnetic permeability, and the minimum torque will increase; therefore, the torque ripple decrease [14].

3.3. Effect of Auxiliary Tooth Deflection on Inductance and Torque

Under the condition of linear assumption, the edge magnetic conductivity effect is ignored, and the leakage of magnetic field is not considered. Fig. 4 shows the simplified diagram of deflection auxiliary tooth, where β_{st1}, β_{st2}, β_{st3} are the arc of stator tooth 1, stator tooth 2, and auxiliary tooth 3, respectively. β_{de} is the auxiliary tooth deflection.

The starting position is defined as the position where the centerline of the motor rotor tooth coincides with the centerline of the groove of stator tooth 1 and stator tooth 2. The magnetic

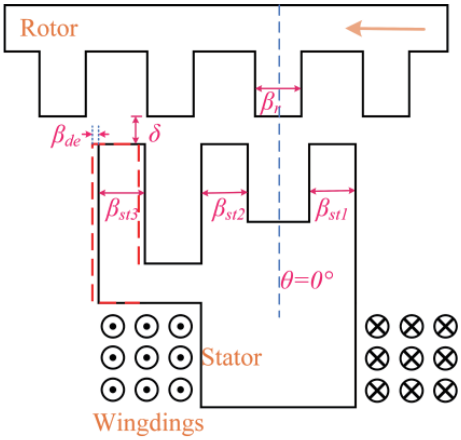

Figure 4. Simplification model for deflection auxiliary teeth.

conductivity from the starting position to the rotor tooth front and the rear edge of stator tooth 1 is analyzed.

The air gap magnetic conductivity differential can be expressed as:

$$d\Lambda = \frac{\mu_0}{\delta} dS = \frac{\mu_0}{\delta} l_s k_\theta R_{ri} w dt = \frac{\mu_0}{\delta} l_s k_\theta R_{ri} d\theta \tag{5}$$

where w is the angular velocity, R_{ri} the inner diameter of the rotor, l_s the axial length of the motor, and k_θ the overlap coefficient of the stator and rotor, which is a function of the rotor position angle. From (3), the magnetic permeability is proportional to the inductance, and we can approximate the change curve of inductance, as shown in Fig. 5., where θ_0 is the critical overlapping position, 0° the starting position, θ_1 the rotor position angle at which the rotor tooth front and auxiliary tooth 3 front just begin to coincide, θ_2 the rotor position angle at which the rotor tooth front and stator tooth 1 front just begin to coincide, θ_3 the rotor position angle at the beginning of the rotor tooth front and the auxiliary tooth 3 trailing edge, and θ_4 the rotor position angle at the beginning of the rotor tooth front and stator tooth 1 trailing edge.

Then, the relationship of inductance and rotor position of the auxiliary tooth deflection structure

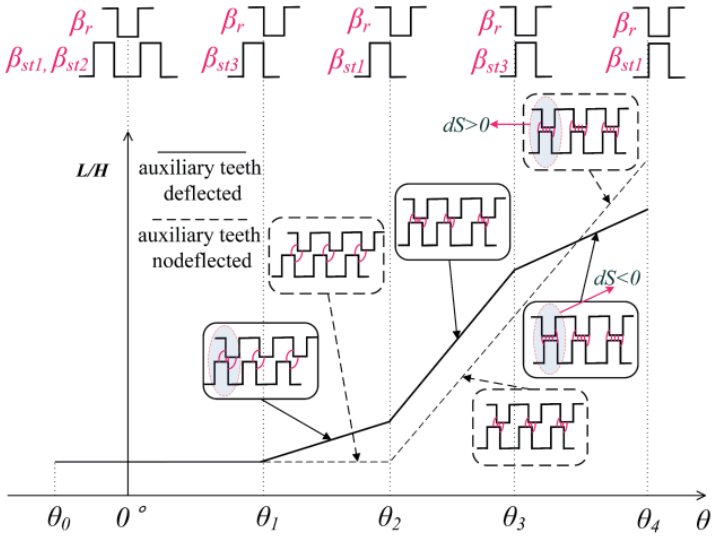

Figure 5. The inductance curves with angle.

at $0^\circ \sim \theta_4$ can be expressed as:

$$L(\theta) = \begin{cases} L_{\min} & 0^\circ \le \theta \le \theta_1 \\ k_{\theta_{1-2}}(\theta - \theta_1) + L_{\min} & \theta_1 \le \theta \le \theta_2 \\ k_{\theta_{2-3}}(\theta - \theta_2) + k_{\theta_{1-2}}(\theta_2 - \theta_1) + L_{\min} & \theta_2 \le \theta \le \theta_3 \\ k_{\theta_{3-4}}(\theta - \theta_3) + k_{\theta_{2-3}}(\theta_3 - \theta_2) + k_{\theta_{1-2}}(\theta_2 - \theta_1) & \theta_3 \le \theta \le \theta_4 \end{cases} \tag{6}$$

where $k_{\theta_{i-j}}$ is the slope of the inductance in the rotor position interval $[\theta_i, \theta_j]$. We select the following special cases to illustrate:

(1) when $\beta_{st1} = \beta_{st2} = \beta_{st3}$, and $\beta_{de} < \beta_{st1}$

$$k_{\theta_{2-1}} \ : \ k_{\theta_{3-2}} \ : \ k_{\theta_{4-3}} = 1 \ : \ 3 \ : \ 1$$

(2) when $\beta_{st1} = \beta_{st2} = \beta_{st3}$, and $\beta_{de} = \beta_{st1}$

$$k_{\theta_{2-1}} \ : \ k_{\theta_{3-2}} \ : \ k_{\theta_{4-3}} = 1 \ : \ 1 \ : \ 1$$

(3) when $\beta_{st1} = \beta_{st2} < \beta_{st3}$, and $\beta_{de} + \frac{\beta_{st3} - \beta_{st1}}{2} = \beta_{st1}$

$$k_{\theta_{2-1}} \ : \ k_{\theta_{3-2}} \ : \ k_{\theta_{4-3}} = 1 \ : \ 2 \ : \ 2$$

Therefore, the inductance change curve can be adjusted by adjusting the 3 arcs of the auxiliary tooth and the deflection angle to achieve the purpose of increasing the minimum torque in the commutation area and reduce the peak torque.

4. OPTIMIZATION DESIGN

4.1. Framework of the Optimization

The optimization design process is divided into four steps. The overall optimization approach framework is shown in Fig. 6. Firstly, we select the optimization objectives and design parameters from the initial

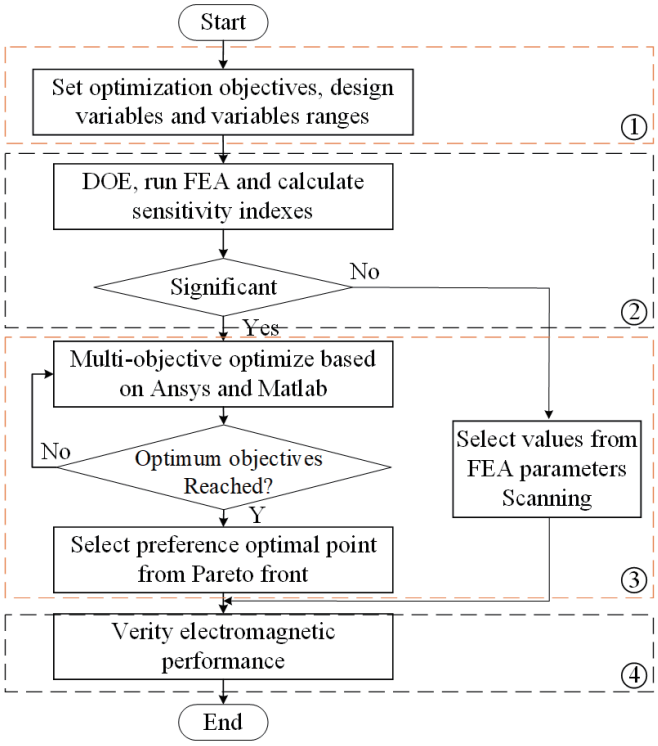

Figure 6. Framework for the multi-objective optimization process.

design. Secondly, the sample space is founded to evaluate the sensitivity of the design parameters on the three design objectives. Sensitivity analysis [15] method is used to screen strongly correlated variables with optimization objectives to reduce the optimization complexity. Thirdly, the strongly correlated variables are optimized by NSGA-II and FEA. Finally, the optimal values can be selected from the real Pareto front solution set of the optimization objectives obtained through the NSGA-II.

4.2. Optimization Objectives and Design

As a power core component of E-bikes, we need to consider its power, driving smoothness, and cruising capability. Therefore, torque ripple (T_{rip}), efficiency (η), and average torque (T_{avg}) are selected as the optimization objectives. The three objectives of ERSRM will be finite element calculated at standard running conditions. The amplitude current is set to 20 A, and the reference speed is set to 350 rpm/min. T_{avg} can be given by:

$$T_{avg} = \frac{1}{t_2 - t_1} \int_{t_1}^{t_2} T dt \tag{7}$$

The efficiency of a switched reluctance motor is obtained by dividing the output power of the motor by the input power, and its expression is:

$$\eta = \frac{P_{out}}{P_{out} + P_{Loss}} \times 100\% \tag{8}$$

$$P_{Loss} = P_{Core\,Loss} + P_{Stranded\,Loss} \tag{9}$$

Based on the specific application, the constraints of ERSRM three objectives are set as follows

$$\begin{cases} T_{rip} \leq 30\%, \quad \eta \geq 80\% \quad T_{avg} > 7\,\mathrm{N \cdot m} \\ P_{out} + P_{loss} < 400\,\mathrm{W} \end{cases} \tag{10}$$

The ERSRM design variables are selected from Table 1 whose values are not determined.

4.3. Parametric Sensitivity Analysis

Firstly, sample space of design parameters and transient field simulation data is founded by Latin hypercubes and FEA. The FEA data is used to assess the linear relationship of design parameters on the three optimization objectives. Pearson correlation coefficient is suitable for expressing this linear relationship which can be given by:

$$\rho_{X_i, Y_{X_i}} = \frac{N \sum X_i Y_{X_i} - \sum X_i \sum Y_{X_i}}{\sqrt{N \sum X_i^2 - \left(\sum X_i\right)^2} \sqrt{N \sum Y_{X_i}^2 - \left(\sum Y_{X_i}\right)^2}} \tag{11}$$

where X_i is the i-th design parameter, Y_{Xi} the optimization objective value corresponding to Xi, and N the total number samples. Based on (11), we calculate the Pearson correlation coefficient of 11 design variables to the three optimization objectives, as given in Fig. 7(a).

When more design parameters are selected, the combination between variables is multiplied, so filtering out the variables that are strongly related to the optimization objectives from these 11 variables to reduce the optimal combination between design variables is necessary. A comprehensive sensitivity analysis is established to quantitatively evaluate the sensitivities of design variables to the three objectives. It is defined as:

$$S_{\mathrm{ERSRM}}(x_i) = w_1 \cdot |S_{Trip}(x_i)| + w_2 \cdot |S_\eta(x_i)| + w_3 \cdot |S_{Tavg}(x_i)| \tag{12}$$

where $S_{\mathrm{ERSRM}}(x_i)$ is the comprehensive sensitivity indices of design parameter x_i, and $|S_{Trip}(x_i)|$, $|S_\eta\ (x_i)|$, and $|S_{Tavg}(x_i)|$ are the absolute Pearson correlation coefficient values of T_{rip}, η, and T_{avg} in ERSRM, respectively. w_1, w_2, and w_3 are the weights of the three objectives. Considering the ERSRM's inherent high torque ripple affects the E-bike driving experience, w_1 is set at 0.5, and w_2 and w_3 are set at 0.25, respectively.

The comprehensive sensitivity index of the 11 design variables to the three optimization objectives can be calculated based on (12), as shown in Fig. 7(b). We incorporated the sensitivity stratification concept into the variable selecting. We set a sensitive threshold $\lambda = 0.15$, and then only six variables of N, θ_{ps}, θ_{st3}, θ_{de}, θ_{on}, and θ_{off} are picked up for subsequent optimization.

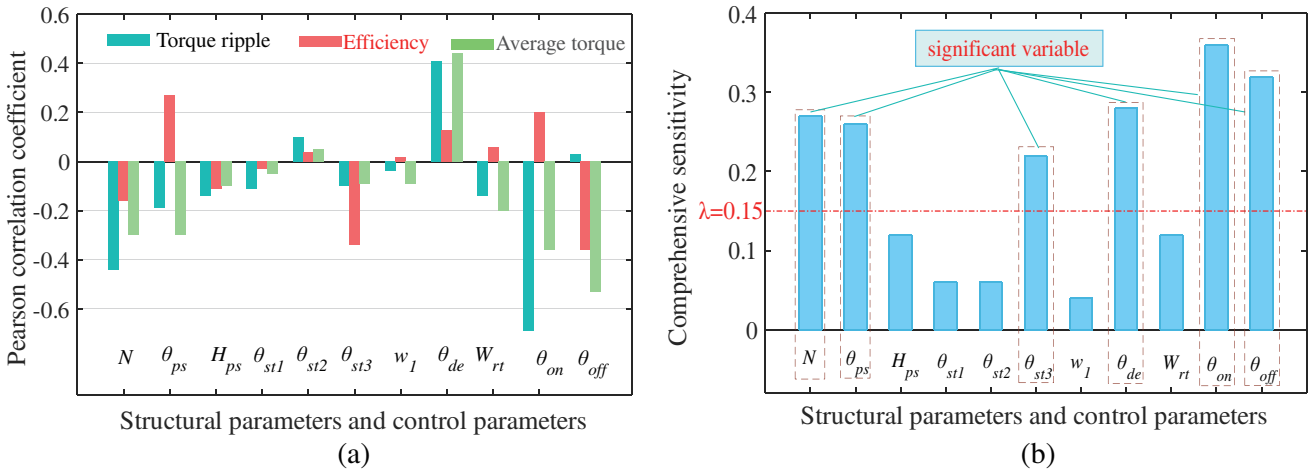

Figure 7. (a) The Pearson correlation coefficient of the 11 parameters to the three optimization objectives. (b) The comprehensive sensitivity of the 11 parameters to the three optimization objectives.

4.4. Multi-Objective Optimization

Many multi-objective evolutionary algorithms (MOEAs) have been used in multi-objective optimization (MOO). Ref. [16] used average torque, torque ripple, and efficiency as performance measures and explored a multi-objective differential evolution (MODE) algorithm combining generalized regression neural network (GRNN), and a comparison of mode with multi-objective genetic algorithm (MOGA) and multi-objective particle swarm optimization (MOPSO) is carried out. The results show that MODE has a better optimization effect than MOGA and MOPSO. However, MODE is defective in its premature convergence. NSGA-II is a global multi-objective optimization algorithm proposed by Deb et al. in [17]. NSGA-II uses tournament system, fast non-dominated sorting approach, and the crowding distance operator which can maintain the global convergence. Therefore, we selected the NSGA-II to optimize the ERSRM.

The traditional optimization method of SRM is to establish the prediction models through historical FEA experimental data. However, the optimization effect of this method is not controllable. There are strong coupling relationships between the design parameters and design parameters, design parameters and performance of SRM, respectively. The optimization results obtained through the prediction model often deviate from the actual simulation values. Therefore, the online optimization method combining algorithm search techniques and transient analysis has received attention from scholars [18]. This method generates the design variables values through the algorithm and then transfers the variables values to the FEA software for simulation through the interface program. After simulation, the performance indicators are transfered to the algorithm for screening to obtain the real Pareto front of the model. The algorithm can automatically correct the evolutionary direction according to the distribution of the Pareto frontier, which constitutes an optimization closed loop. So, we use the Maxwell simulation software to obtain the performance indicators of ERSRM, and Visual Basic script program is used to transfer the design parameters and FEA results. Multi-objectives optimization of ERSRM is achieved by the NSGA-II. The framework of ERSRM optimization process based on NSGA-II is given in Fig. 8.

Based on the above work, the NSGA-II algorithm was run for 50 generations using a population size of 30. The recombination and mutation parameters are set to 0.8 and 0.2, respectively.

Figure 9 shows the obtained 3-D Pareto front and all studied points and projection plots of the Pareto front into 2D. The differences between the parameters and performances of the initial motor and optimal motor are shown in Table 2.

It can be seen from Table 2 that although the efficiency of optimized motor has decreased by 3.16%, the average torque has increased by 6.25%, and the torque ripple has decreased by 86.58% compared with the motor of the initial design. The torque ripple was significantly reduced.

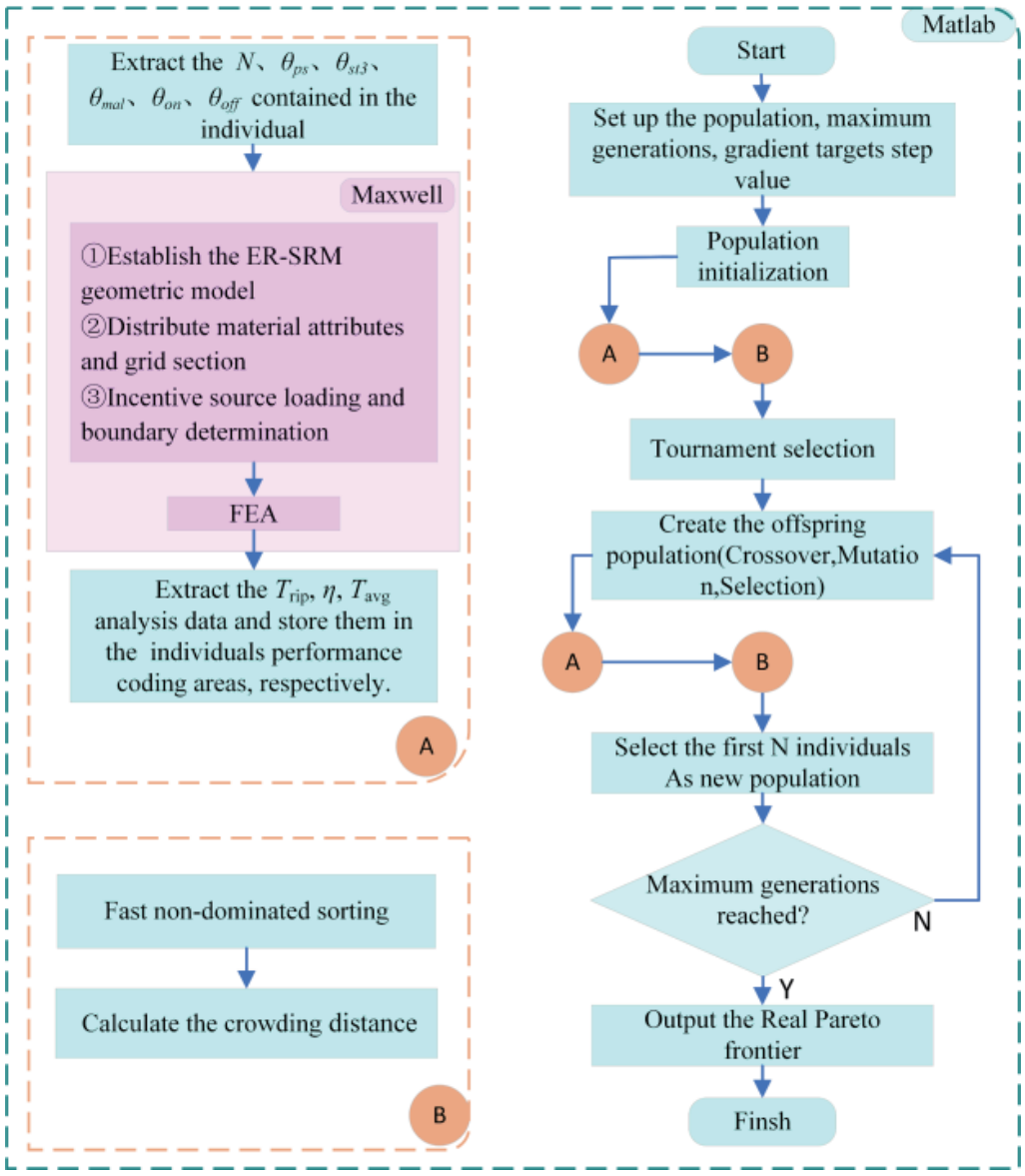

Figure 8. The process of ERSRM optimization based on NSGA-II.

5. COMPARISON OF MOTOR PERFORMANCES

Figures 10(a), 10(b), and 10(c) show the comparison of transient torque, comparison of single-phase torque, and comparison of single-phase current with inductance of the optimal and initial motor 6, respectively. From Fig. 10(b), the single-phase torque has partial negative torque. That is because the single-phase current does not decrease to 0 in the inductance drop area with the delay of the θ_{off}. The negative torque is also the partial reason for the reduction of motor efficiency.

We decompose the optimized motor backwards for analysis and decompose it into two parts: the motor with pole shoes and the motor with deflection auxiliary teeth, as shown in Fig. 11. The simulation comparison results of different structures are shown in Fig. 12 and Fig. 13, respectively.

From Fig. 12(a), the motor with pole shoes possesses higher average torque and lower torque ripple than the symmetrical motor in the case of constant rotor size. From the perspective of A-phase-torque, the transient torque of the motor with pole shoes in the $[-1°, 4.49°]$ turn-on interval is greater than

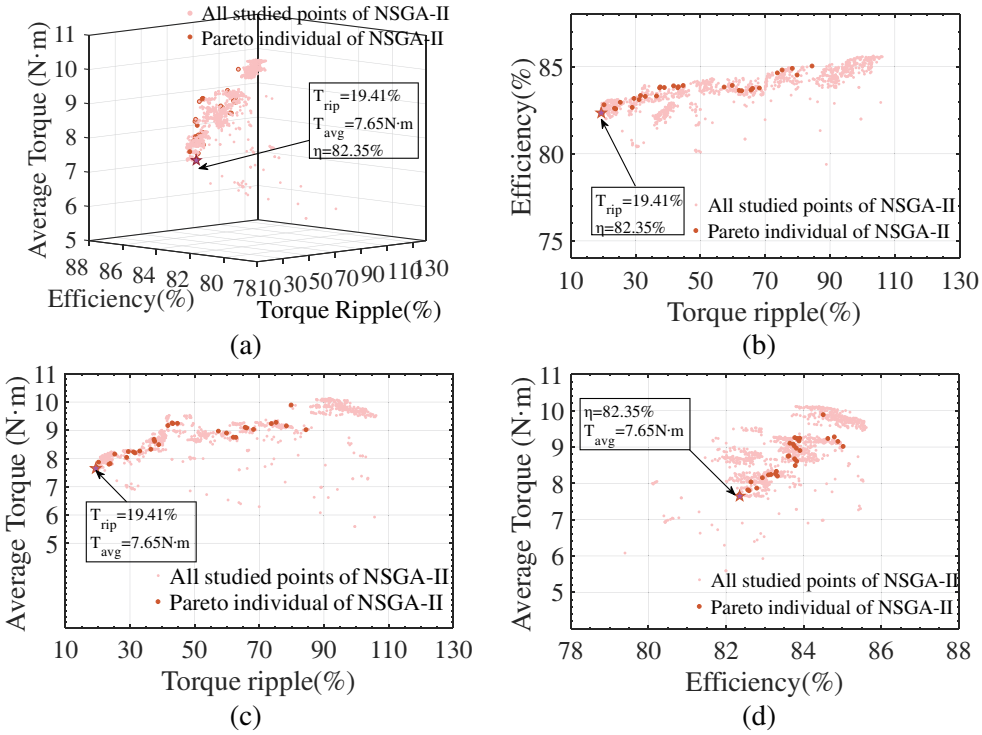

Figure 9. Pareto frontier. (a) 3-D Pareto frontier of NSGA-II. (b) Torque ripple versus efficiency. (c) Torque ripple versus average torque. (d) Efficiency versus average torque.

Table 2. Design variables and performance of initial and optimal.

	Parameters	Initial	optimal
Motor parameters	N	38	39
	θ_{ps} (°)	1	2.2
	H_{ps} (mm)	1.5	1.5
	θ_{st1} (°)	4.5	4.5
	θ_{st2} (°)	4.5	4.5
	θ_{st3} (°)	5	7.95
	W_1 (mm)	5.6	5.6
	θ_{de} (°)	−1	−2.41
	W_{rt} (mm)	7.2	7.2
	θ_{on} (°)	0	−0.9
	θ_{off} (°)	6	7.6
Output performance	$P_{coreloss}$ (W)	25.56	32.98
	$P_{strandedloss}$ (W)	19.35	27.11
	T_{rip} (%)	144.67	19.41
	η (%)	85.78	82.35
	T_{avg} (N · m)	7.39	7.65

the symmetrical motor. From Fig. 12(b), adding pole shoes improves the inductance in the entire conduction zone. Meanwhile, the rotor position angle of the motor with pole shoes is delayed by 0.14° compared to the symmetrical motor when the A-phase-current reaches the current limit for the first

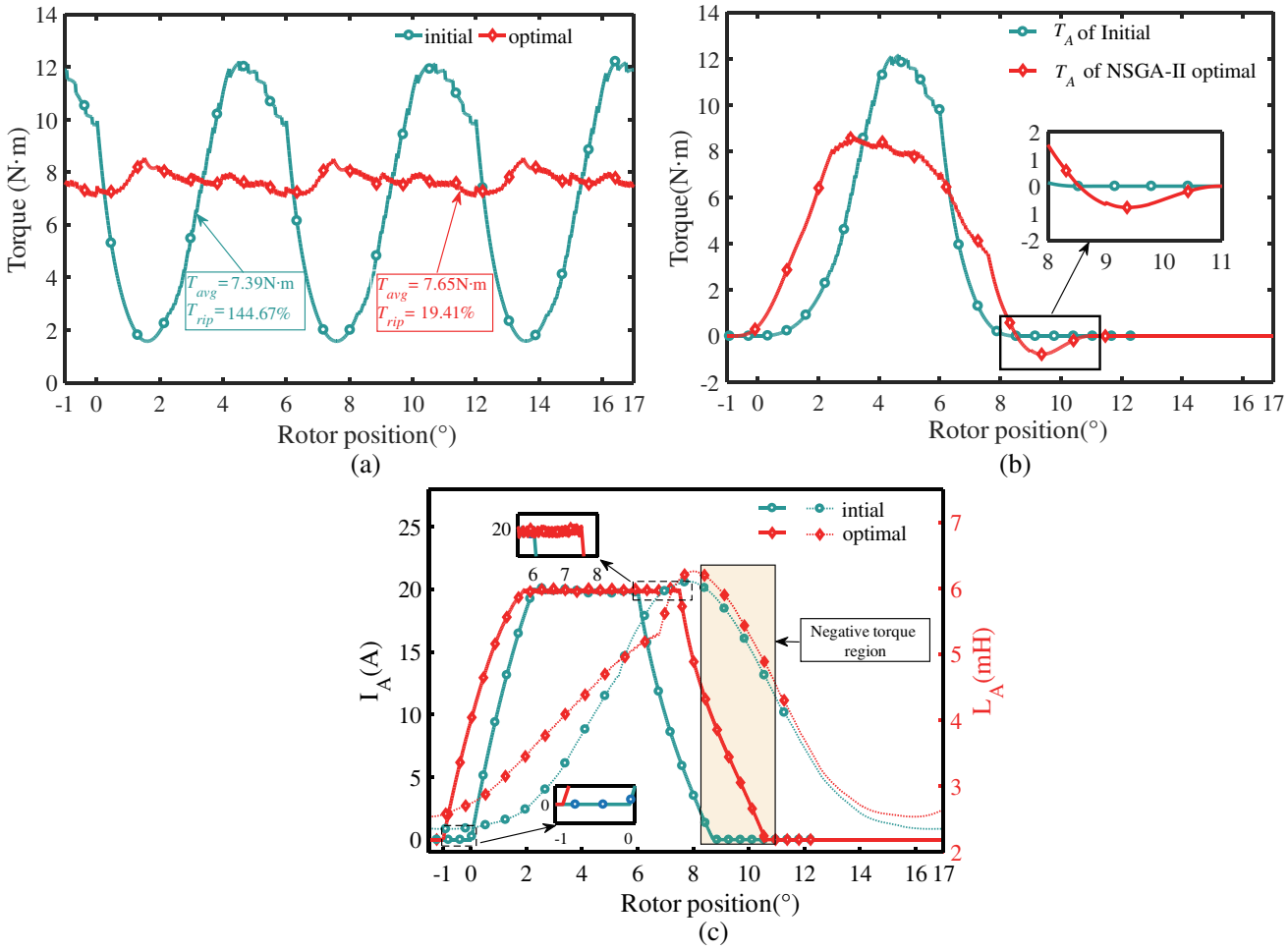

Figure 10. (a) Comparison of transient torque. (b) Comparison of single-phase torque. (c) Comparison of single-phase current with inductance.

time, which is due to the increase of the A-phase-inductance in the early turn-on interval.

From Fig. 13(a), the motor with deflection auxiliary teeth possesses lower average torque and lower torque ripple than the motor with no-deflection auxiliary teeth in the case of constant rotor size. From the perspective of A-phase-torque, the transient torque of the motor with deflection auxiliary teeth in the $[-1°, 2.77°]$ turn-on interval is greater than the motor with no-deflection auxiliary teeth. From Fig. 13(b), the deflection of auxiliary teeth improves the A-phase-inductance in the early turn-on interval, but the maximum of A-phase-inductance is reduced. Meanwhile, the rotor position angle of the motor with deflection auxiliary teeth is delayed by 0.5° compared to the motor with no-deflection auxiliary teeth when the A-phase-current reaches the current limit for the first time, which is due to the increase of the A-phase-inductance in the early turn-on interval.

In conclusion, the combined structure of the pole shoe and the deflection auxiliary tooth increases the minimum synthetic torque and reduces the torque peak, which makes the torque ripple significantly reduced.

6. EXPERIMENTAL VERIFICATION

The experiment prototype is manufactured according to structural parameters contained in the selected optimal solution. The rotor, stator, structure diagram, and experimental platform are shown in Fig. 14. Three bearings are installed in the motor. Two small bearings fix the shaft in the axial and radial

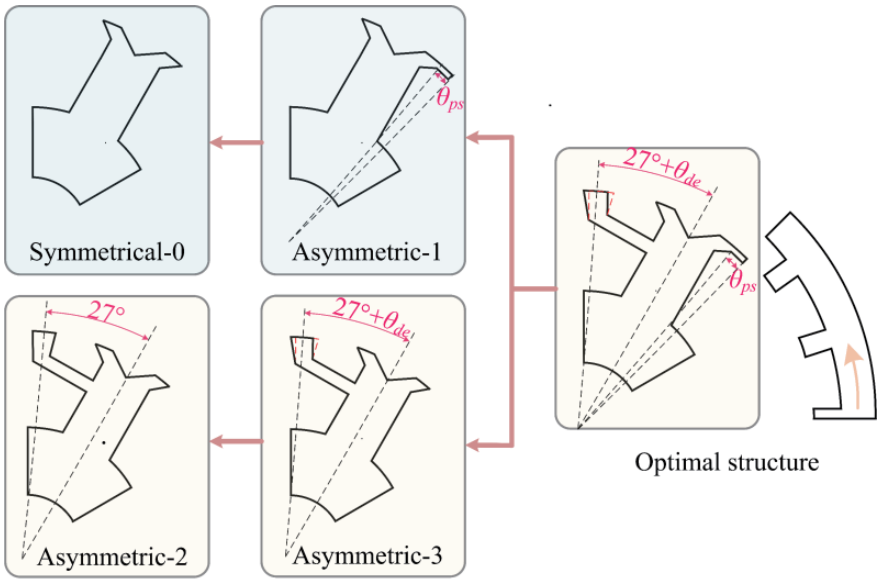

Figure 11. Reverse decomposition of optimized structures.

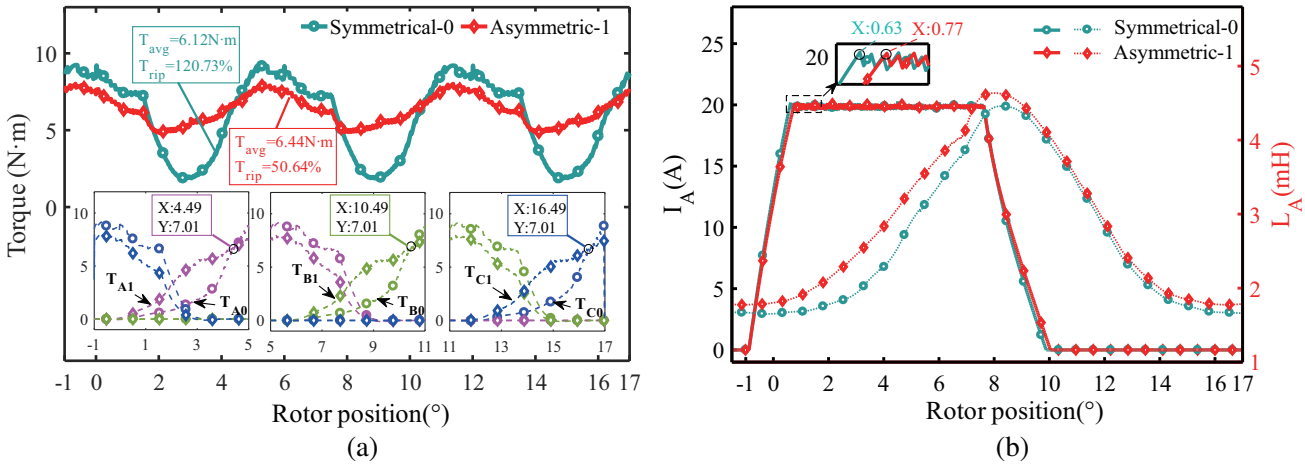

Figure 12. (a) Comparisons of transient torque and single-phase torque. (b) Comparison of single-phase current and inductance.

directions, and the radial displacement of the rotor housing can be reduced by large bearings on the outside. We connect the rotor and the shaft together via a connecting-shaft iron block to measure the torque data. TMS320F28335DSP is used to output control signals, and the rotor position angle is converted by the absolute encoder signal.

The prototype operates under angle position control (APC). The amplitude of phase current is 20 A; the turn on angle is $-0.9°$; and the turn off angle is 7.6°. It can achieve a steady load by adjusting the excitation current of the magnetic powder tension controller. The torque ripple data and speed change data under different load are shown in the Fig. 15(a) and Fig. 15(b).

As shown in Fig. 15(a), the torque ripple reaches the maximum at a load of $0.5\,\mathrm{N}\cdot\mathrm{m}$, and the value is 20%. The torque ripple then decreases as the load increases, reaching the minimum value at a load of $4\,\mathrm{N}\cdot\mathrm{m}$. When the load is in the range of $0\,\mathrm{N}\cdot\mathrm{m} \sim 6\,\mathrm{N}\cdot\mathrm{m}$, the torque ripple under different loads is small after stable operation. As shown in Fig. 15(b), the speed fluctuation is small and can quickly respond to the rated speed after the load changes.

When the prototype operates under the rated parameters, the current and output electromagnetic

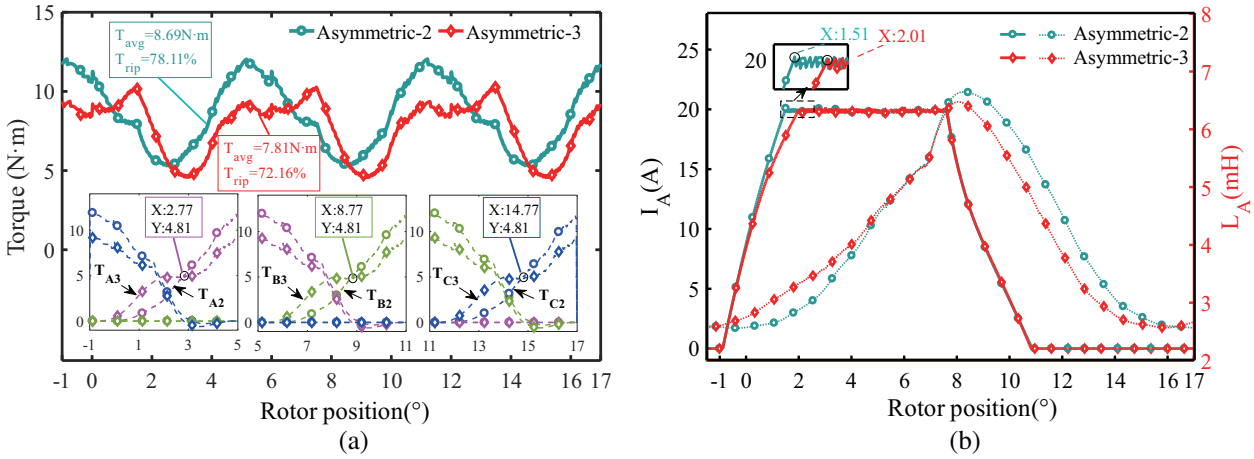

Figure 13. (a) Comparisons of transient torque and single-phase torque. (b) Comparison of single-phase current and inductance.

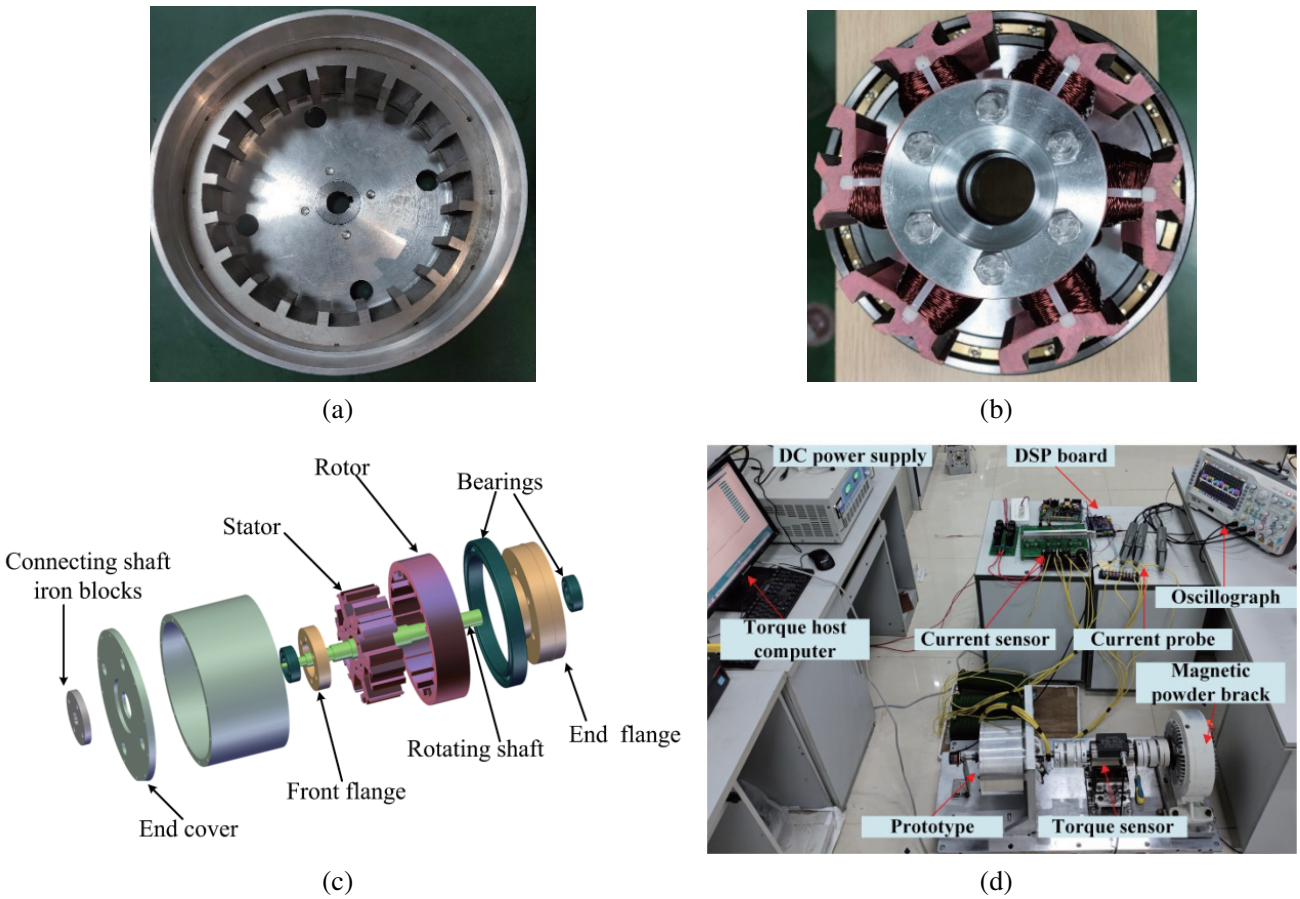

Figure 14. (a) Rotor. (b) Stator. (c) The structure diagram of ERSRM. (d) Experimental platform.

torque of the motor are shown in Fig. 16(a) and Fig. 16(b), respectively. The output torque is smaller than the simulation value, and the torque ripple is about 10.57%. The difference between FEA-predicted torque ripples and measured ones can be attributed to the end effect ignorance in FEA, the manufacturing tolerance, the actual installation error, and the control response accuracy.

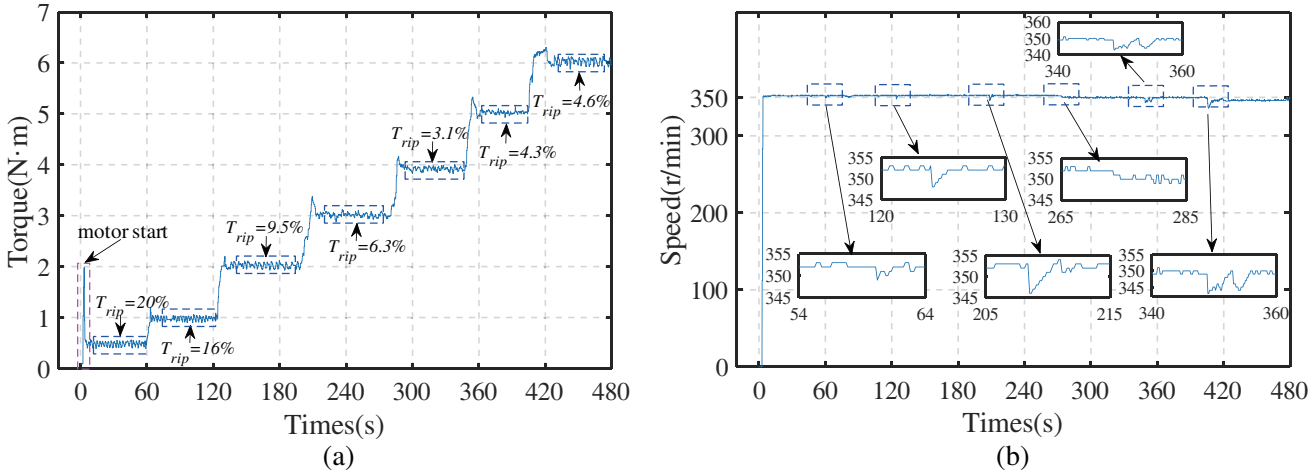

Figure 15. (a) Torque ripple data under different load. (b) Speed change data under different load.

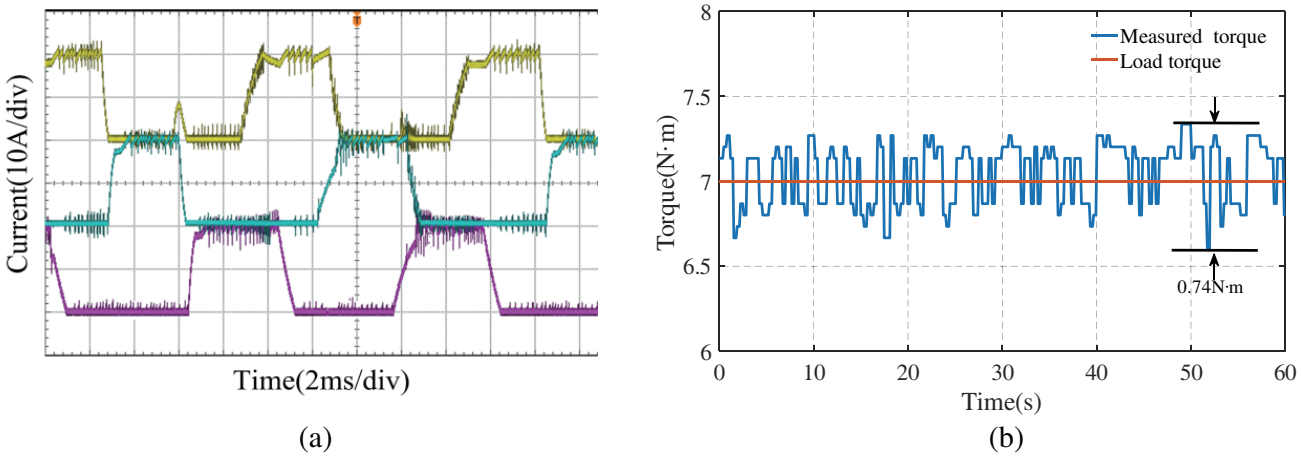

Figure 16. (a) Current experimental result. (b) Torque experimental result.

7. CONCLUSION

In this paper, a multi-objective optimal design for the ERSRM with asymmetric stator poles is investigated. The torque ripple, efficiency, and average torque are considered as the optimization objectives. The FEA results show that the optimal motor has a higher average torque and lower torque ripple than the initial motor. The torque ripple of the optimal motor is reduced by 86.58%. Then the experiment prototype is manufactured according to the selected optimal solution. The optimal motor torque has been measured experimentally, and the results show that the asymmetric structure has a good suppression effect on torque ripple.

ACKNOWLEDGMENT

This work was supported by the National Natural Science Foundation of China under Project 52167005.

REFERENCES

1. Howey, B., B. Bilgin, and A. Emadi, "Design of an external-rotor direct drive E-bike switched reluctance motor," *IEEE Transactions on Vehicular Technology*, Vol. 69, No. 3, 2552–2562, 2020.

2. Ahn, J. W. and G. F. Lukman, "Switched reluctance motor: Research trends and overview," *CES Transactions on Electrical Machines and Systems*, Vol. 2, No. 4, 339–347, 2018.
3. Anvari, B., H. Toliyat, and B. Fahimi, "Simultaneous optimization of geometry and firing angles for in-wheel switched reluctance motor drive," *IEEE Transactions on Transportation Electrification*, Vol. 4, No. 1, 322–329, 2018.
4. Zhu, J. W. K., W. E. Cheng, and X. D. Xue, "Torque analysis for in-wheel switched reluctance motors with varied number of rotor poles," *International Symposium on Electrical Engineering (ISEE)*, Hong Kong, China, Dec. 20, 2016.
5. Arifin, A., I. Al-Bahadly, and S. Mukhopadhyay, "Performance analysis of a 12/8 and 12/16 switched reluctance machine in low and medium speed operations for wind energy applications," *2012 IEEE International Conference on Power And Energy (PECON)*, 916–921, 2012.
6. Balaji, M., S. Ramkumar, and V. Kamaraj, "Sensitivity analysis of geometrical parameters of a switched reluctance motor with modified pole shapes," *Journal of Electrical Engineering and Technology*, Vol. 9, No. 1, 136–142, 2014.
7. Mehta, S., M. A. Kabir, P. Pramod, et al., "Segmented rotor mutually coupled switched reluctance machine for low torque ripple applications," *IEEE Transactions on Industry Applications*, Vol. 57, No. 4, 3582–3594, 2021.
8. Lee, C., J. Lee, and I. G. Jang, "Shape optimization-based design investigation of the switched reluctance motors regarding the target torque and current limitation," *Structural and Multidisciplinary Optimization*, Vol. 64, No. 2, 859–870, 2021.
9. Mariappan, G. and K. Lakshmanan, "An enhanced control method for torque ripple minimization of switched reluctance motor using hybrid technique," *Journal of Intelligent & Fuzzy Systems*, 1–24, 2022.
10. Fatih, K., T. Ismail, M. Hayati, et al., "Reduction of torque ripple in induction motor by artificial neural multinetworks," *Turkish Journal of Electrical Engineering and Computer Science*, Vol. 24, No. 5, 3492–3502, 2016.
11. Pan, Z. B. and S. H. Fang, "Combined random forest and NSGA-II for optimal design of permanent magnet arc motor," *IEEE Journal of Emerging and Selected Topics in Power Electronics*, Vol. 10, No. 2, 1800–1812, 2022.
12. Hua, Y. Z., H. Q. Zhu, M. Gao, Z. Ji, et al., "Multi-objective optimization design of permanent magnet assisted bearingless synchronous reluctance motor using NSGA-II," *IEEE Transactions on Industrial Electronics*, Vol. 68, No. 11, 10477–10487, 2020.
13. Mohamed, E., A. Mohamed, R. Hegazy, and N. I. Mohamed, "Finite element based overall optimization of switched reluctance motor using multi-objective genetic algorithm (Nsga-II)," *Mathematics*, Vol. 9, No. 5, 1–20, 2021.
14. Ma, H. Z., C. Z. Huang, X. P. Liu, et al., "The effect of a single-sided pole shoe and slot on reducing torque ripple in a switched reluctance motor," *Concurrency Computation*, Vol. 32, No. 19, e5810, 2020.
15. Wang, X., L. Yuan, H. Chen, et al., "Sensitivity analysis on novel U-shape dual-stator switched reluctance motor," *IEEE Transactions on Applied Superconductivity*, Vol. 31, No. 8, 1–5, 2021.
16. Nagarajan, V. S., B. Mahadevan, et al., "Design optimization of ferrite assisted synchronous reluctance motor using multi-objective differential eVolution algorithm," *COMPEL: The International Journal for Computation and Mathematics in Electrical and Electronic Engineering*, Vol. 36, No. 1, 219–239, 2017.
17. Deb, K., A. Pratap, S. Agarwal, and T. Meyarivan, "A fast and elitist multiobjective genetic algorithm: NSGA-II," *IEEE Transactions on Evolutionary Computation*, Vol. 6, No. 2, 182–197, 2002.
18. Huang, C. Z., H. W. Yuan, Y. L. Wu, et al., "A preference multi-objective optimization method for asymmetric external rotor switched reluctance motor," *Progress In Electromagnetics Research C*, Vol. 124, 179–196, 2022.